Nanoelectronics and Its New Materials – A NEW ERA OF NANOSCIENCE

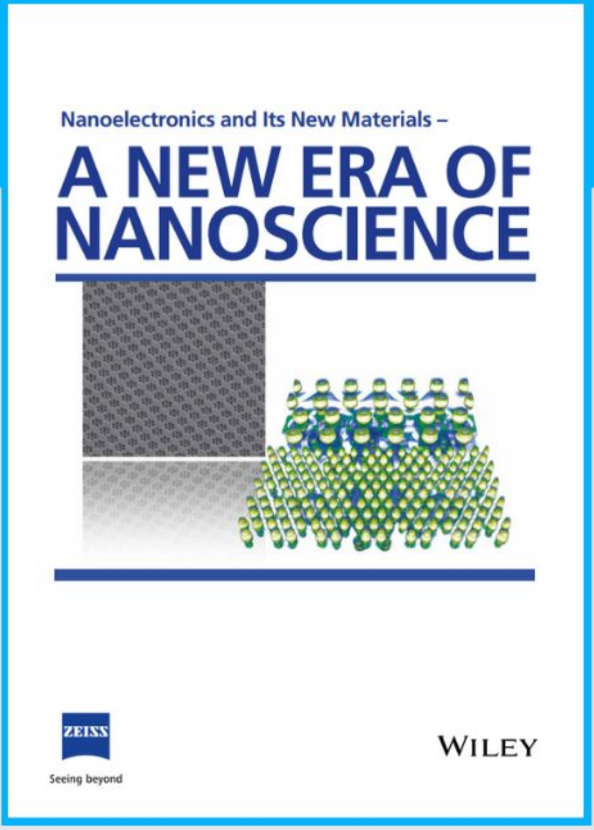

Nanoelectronics and Its New Materials –

A NEW ERA OF NANOSCIENCE

ZEISS

Seeing beyond

WILEY

Discover the recent advances in electronics research and fundamental nanoscience.

Nanotechnology has become the driving force behind breakthroughs in engineering, materials science, physics, chemistry, and biological sciences. In this compendium, we delve into a wide range of novel applications that highlight recent advances in electronics research and fundamental nanoscience. From surface analysis and defect detection to tailored optical functionality and transparent nanowire electrodes, this eBook covers key topics that will revolutionize the future of electronics.

To get your hands on this valuable resource and unleash the power of nanotechnology, simply download the eBook now. Stay ahead of the curve and embrace the future of electronics with nanoscience as your guide.

ZEISS

Seeing beyond

WILEY

physica status solidi a
www.pss-a.com

Controlling In-Plane Magnetic Anisotropy of Co Films on MgO Substrates using Glancing Angle Deposition

*Andreas Frisk, Barat Achinuq, David G. Newman, Emily Heppell, Maciej Dąbrowski, Robert J. Hicken, Gerrit van der Laan, and Thorsten Hesjedal**

The ability to control the in-plane magnetic anisotropy of a thin film is important for magnetic device applications. One way of accomplishing this task is by glancing angle deposition (GLAD). Herein, thin Co layers have been deposited using GLAD magnetron sputtering on MgO(001) and MgO(110) substrates. For Co films on MgO(001), the in-plane anisotropy direction can be directly controlled via the deposition angle. In contrast, for Co on MgO(110), the anisotropy due to the deposition angle competes with the anisotropy induced by the substrate, while the growth parameters determine which contribution dominates. On the other hand, while on MgO(001) the deposition angle as well as the film thickness affect the strength of the Co in-plane anisotropy, no influence of these parameters on the magnetic properties is found for films on MgO(110).

1. Introduction

Magnetic anisotropy is a key property of thin magnetic films, and its control is crucial for device applications,[1,2] e.g., for spin-valves in which the magnetization direction determines the state of the device,[3–5] as well as for designing skyrmion-hosting heterostructures,[6] to name a few examples. Magnetic anisotropy has essentially two distinct origins, namely a macroscopic one due to, e.g., grain boundaries, and a microscopic one due to the electronic structure, as induced by the orbital moment anisotropy and magnetic dipole term.[7] Common ways of controlling the anisotropy are via the choice of crystal orientation of the substrate[8] or overlayer,[9] the film thickness,[10] or the surface morphology,[11–14] which can be engineered in clever ways.[15] Another way of accomplishing in-plane anisotropy control is by using glancing angle deposition (GLAD).[16–18] The principle of the technique is as follows:[19–21] when a film is deposited at a small, glancing angle, i.e., not under normal incidence as usual in thin film deposition, the incoming atoms will deposit preferentially on the side of the grains facing the deposition source. This so-called shadow effect will result in tilted columnar growth, with the columns tilting toward the deposition source. This structural uniaxial anisotropy will, in turn, affect the magnetic anisotropy, whereby the direction toward the deposition source will either become the hard or the easy axis. The dependence of the anisotropy energy on the deposition angle and the thickness has been reported for GLAD films,[16,22] with a switch of the easy axis direction from parallel to perpendicular to the growth direction. So far, most of the GLAD growth has been carried out on amorphous substrates, such as plastic or glass,[22] which is useful for high-density recording tapes. However, for magnetic device applications, and in general for the integration with functional layers, the GLAD films have to be deposited onto crystalline substrates or layers. The effect of the crystal structure of the substrate or underlayer on GLAD growth has not been investigated in detail before.

The combination of ferromagnetic layers with large spin–orbit coupling and dielectric materials is particularly promising for exploring all-electric device schemes for magnetic random-access memory applications.[23,24] While the combination of a heavy metal such as Pt and a ferromagnetic layer such as Co exhibits an efficient charge-to-spin conversion efficiency[25] and enables current-induced spin–orbit torque switching of an adjacent Co layer,[26] the proximity to an MgO layer induces perpendicular magnetic anisotropy in the Co layer.[27] This material combination also allows for a tuning of its energy terms, enabling the nucleation of magnetic skyrmion bubbles.[28] Here, we report the investigation on the ability of GLAD to control the anisotropy of Co films on Pt-coated MgO(001) and lower symmetry MgO(110) substrates. We carried out structural and magnetic studies to

---

A. Frisk, G. van der Laan
Diamond Light Source
Harwell Science and Innovation Campus
Didcot, Oxfordshire OX11 0DE, UK

B. Achinuq, E. Heppell, T. Hesjedal
Department of Physics
University of Oxford
Parks Road, Oxford OX1 3PU, UK
E-mail: Thorsten.Hesjedal@physics.ox.ac.uk

D. G. Newman, M. Dąbrowski, R. J. Hicken
Department of Physics and Astronomy
University of Exeter
Stocker Road, Exeter, Devon EX4 4QL, UK

The ORCID identification number(s) for the author(s) of this article can be found under https://doi.org/10.1002/pssa.202300010.

DOI: 10.1002/pssa.202300010

correlate the microstructure with the magnetic anisotropy. We found that whereas on the (001) surface the deposition conditions fully control the magnetic properties of a Co film, the (110)-surface-induced anisotropies dominate over the deposition-induced effects.

2. Experimental Section

2.1. The GLAD Process

The samples were grown by GLAD in a home-built, eight-source magnetron sputter deposition system (top view of the chamber is shown in **Figure 1**a, and the sample geometry is shown in Figure 1b). Five of the sources are mounted in the horizontal plane, while Pt and Co are 17° below the horizontal plane, having their focus in the center of the chamber.

The deposition geometry is illustrated in Figure 1b. The substrate is mounted in the center of the chamber and it has two axes of rotation, φ_S around the (vertical) z-axis and θ_S around the surface normal (of the substrate) $\mathbf{N}_S$ (for example, $\theta_S = 90°$, rotating the substrate axis from $\mathbf{S}_2$ to $\mathbf{S}_1$). The angles relevant for the film growth, α and β, are shown in Figure 1b and are defined as follows: α_i is the angle between the substrate normal $\mathbf{N}_S$ and the direction to the ith deposition source (position vector $\mathbf{M}_i$), i.e., $(90° - \alpha_i)$ is the incident deposition angle onto the sample (the *GLAD angle*); p_i is the projection of $\mathbf{M}_i$ onto the sample plane, and β is the angle between the coordinate axis of the substrate S_1 and the projected vector $\mathbf{p}_i$. In other words, β is the in-plane direction of deposition, i.e., the *imprinting angle*. Both α and β can be chosen via the azimuthal φ_S and polar θ_S substrate rotations. A more detailed discussion of the dependence of thin film magnetron sputtering on the deposition geometry can be found in Chapter 6 in ref. [29].

The samples investigated here were mounted such that $\beta = 0°$ is parallel to the $\langle 001 \rangle$ direction of MgO(110) and parallel to $\langle 100 \rangle$ of MgO(001), respectively. In the right panel of Figure 1, a top-down view of a MgO(110) substrate is shown to clarify the angle β. In the illustrated example, the imprinting angle of $\beta = 13°$ is achieved by a sample rotation of $\theta_S = 30°$. It also shows the definition of the angle φ_H, i.e., the direction of the applied (in-plane) magnetic field $\boldsymbol{H}$ for the characterization experiments conducted on the samples. Here, the example of $\varphi_H = 60°$ is shown. By definition, for $\varphi_H = 0°$ and $\beta = 0°$, the imprinting direction and the direction of the applied field coincide. The geometry of GLAD-induced columnar growth, along with all relevant angles and orientations, is illustrated in **Figure 2**.

2.2. Sample Growth

Pt/Co/Pt thin film trilayers were deposited on MgO(001) and MgO(110) substrates using DC magnetron sputtering. The films were deposited in an ultrahigh vacuum chamber, with a base pressure $< 4 \times 10^{-9}$ mbar, using 99.999% pure Ar as a sputtering gas at a pressure of $\approx 2 \times 10^{-3}$mbar. Prior to growth, the substrates were baked in UHV at 650 °C for 3 h. The substrates were left to cool to room temperature before a Pt layer was deposited with a deposition rate of 0.19 Å s^{-1} (and a thickness on the order of 10 Å; see respective sample description, e.g., in **Figure 3** for precise value). This layer was deposited at "normal incidence" for cosputtering conditions (i.e., with $\alpha_{Pt} = 17°$) and with continuous rotation around the substrate normal, which resulted in epitaxial growth of Pt. Subsequently, a Co layer was deposited under GLAD conditions with varying $\alpha_{Co} = 80°$, 60°, 67°, 50°; $\beta_{Co} = 0°$, 30°, 60°; and thicknesses from 20 to 500 Å. An effective deposition rate of $0.16 - 0.27$ Å s^{-1} was used depending on α, corresponding to a deposition rate of 0.44 Å s^{-1} for deposition under normal incidence ($\alpha = 0°$). Finally, the sample was capped with a nominally 10 Å-thick Pt layer (at $\alpha_{Pt} = 17°$ and using continuous sample rotation) to protect against oxidation.

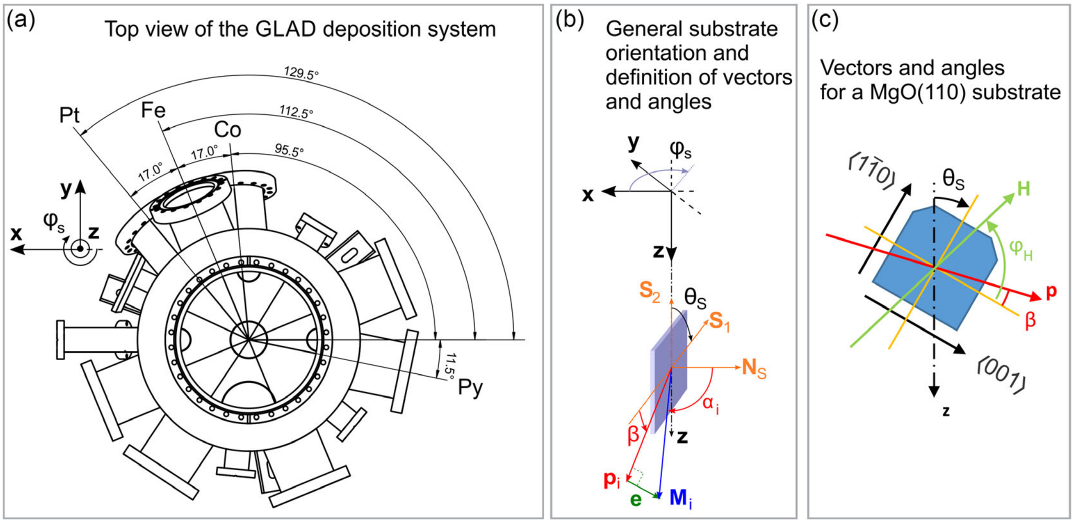

Figure 1. a) Top view of the magnetron sputtering chamber showing the positions of the eight magnetrons arranged in the *x*-*y* source plane around the sample manipulator axis (*z* axis). b) Orientation of the substrate in the reference frame of the chamber with φ_S being the rotation around the *z*-axis and θ_S around the surface normal (of the substrate) $\mathbf{N}_S$. The deposition sources are located at $\mathbf{M}_i$, i.e., at an angle α_i away from the surface normal $\mathbf{N}_S$. Consequently, $(90° - \alpha)$ is the GLAD angle and β the in-plane deposition angle. c) Geometry for a MgO(110) substrate with the angles defined relative to its crystallographic axes.

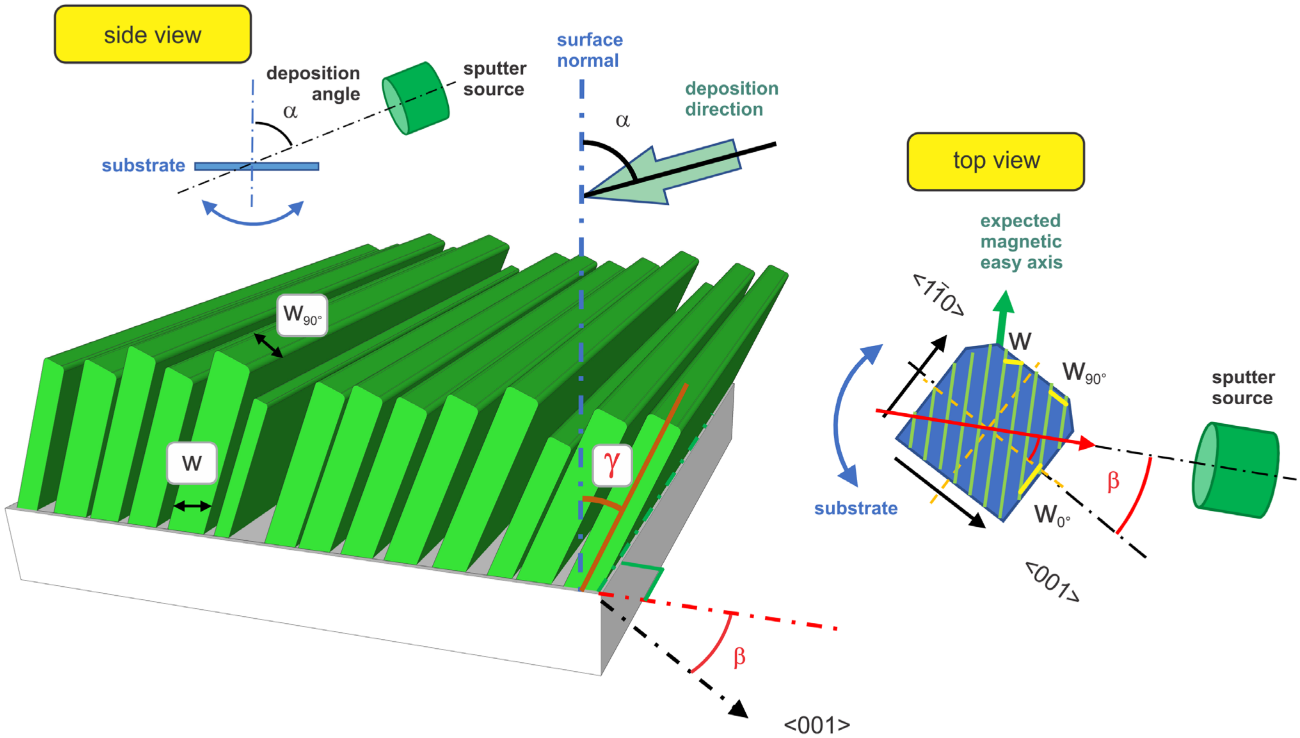

Figure 2. Schematic of the microstructure of a sample, showing columnar growth features with tilting angle γ and real and projected widths w and w_{90°, respectively. On the left, a side view, and on the right, a top view is shown [for a MgO(110) substrate]. In an imprinting scenario, the in-plane deposition angle β determines the direction of the magnetic easy axis (to be perpendicular to it).

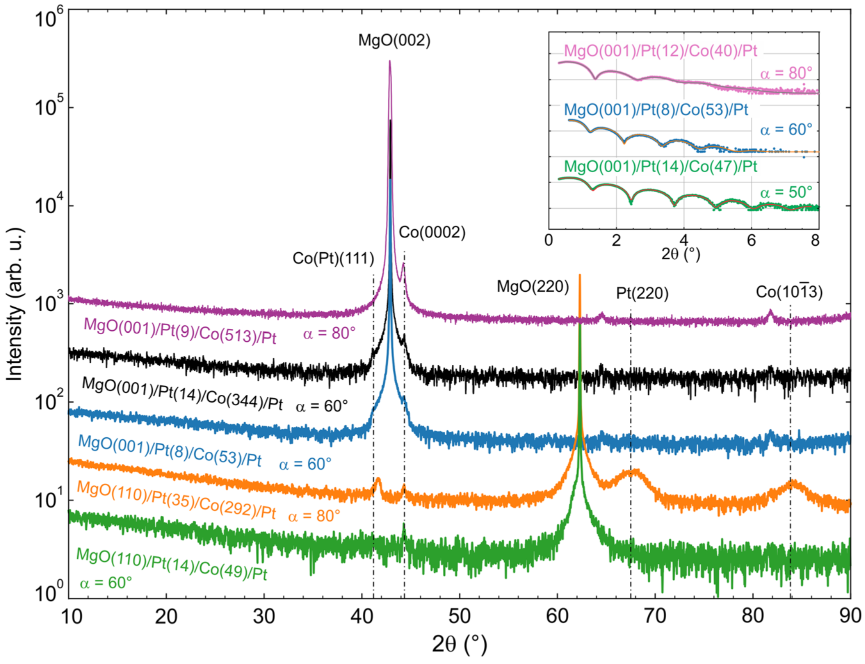

Figure 3. Out-of-plane XRD ($\omega - 2\theta$) scans with Cu Kα radiation. Above, the result for heterostructures on MgO(001) substrates are shown, i.e., Pt(9)/Co(513)/Pt (thicknesses in Å) in purple ($\alpha = 80^\circ$), Pt(14)/Co(344)/Pt in black and Pt(8)/Co(53)/Pt in blue (both $\alpha = 60^\circ$). Below, results for a thicker (in orange; $\alpha = 80^\circ$) and a thinner (in green; $\alpha = 60^\circ$) heterostructure on MgO(110) are plotted. On both samples on MgO(110), imprinting was not successful. In the thicker heterostructure ($d_{\mathrm{Pt}}^{\mathrm{buffer}} = 35$ Å), the Pt underlayer is clearly epitaxial with Pt[220]||MgO[220]. The inset shows XRR data on selected samples with a Co thickness of ≈50 Å. The Pt cap layer thickness was ≈10 Å.

2.3. Structural and Magnetic Sample Characterization

2.3.1. XRR and XRD

A Rigaku Smart Lab X-ray diffractometer was used to measure X-ray reflectivity (XRR) and various types of X-ray diffraction (XRD) patterns using Cu Kα radiation. The XRR data were fitted using GenX.[30] Out-of-plane diffractograms (ω-2θ scans), as well as pole figures of selected reflections, were recorded to determine the epitaxial relationships of the Pt and Co layers and the MgO substrate.

2.3.2. Magnetometry

In-plane hysteresis loops were measured at room temperature on a MicroSense vibrating sample magnetometer (VSM) capable of bias fields up to $\pm 1.8\,\text{T}$. The samples were mounted on a quartz rod that was rotated through various in-plane angles φ_H, allowing for the angular dependence of the remanent magnetization to be determined. Hysteresis loop data points were averaged five times, except for the thinner samples with $d_{Co} \le 50\,\text{Å}$ where the average was over 15 data points to improve the signal-to-noise ratio.

2.3.3. Electron Microscopy

Cross-sectional transmission electron microscopy (TEM) samples were prepared both by focused-ion-beam (FIB) milling in a JIB-4700F Multi Beam System and by conventional methods that include mechanical thinning and Ar ion milling. Structural studies were performed by TEM imaging in a JEOL JEM-2100 microscope operated at 200 kV. Prior to the FIB preparation, the samples were sputter-coated with a ≈20 mm-thick Au film to protect the sample from beam damage as well as to reduce charging.

3. Results and Discussion

3.1. Structural Properties

Out-of-plane XRD (Figure 3) for films on MgO(001) shows, apart from the substrate peak, weak hcp Co(0002) and either fcc Co or CoPt (111) reflections at $2\theta = 44.4°$ and 41.2°, respectively. The lack of other reflections for films on MgO(001) shows that there is no dominant crystalline order along the out-of-plane direction. This behavior is independent of the Co film thickness (from 20 to 500 Å). In contrast, samples on MgO(110) also show reflections that can be attributed to an epitaxial Pt(220) layer ($2\theta = 67.5°$), as well as three Co reflections. First, at $2\theta = 44.4°$, there is the hexagonal Co(0002) peak, then at 41.2° possibly the (111) peak of either fcc Co or CoPt, and lastly at 83.8° the hexagonal Co($10\bar{1}3$) peak.

We used XRR to determine the thicknesses of the grown layers. We confirmed that the layer thicknesses match the nominal values of $d_{Pt}^{buffer\&cap} = 13\,\text{Å}$ and the stated d_{Co} within the uncertainties, taking the interfacial roughness into account. The roughnesses are on average $\sigma_{Pt}^{buffer} = 5\,\text{Å}$, $\sigma_{Co} = 5$ to $35\,\text{Å}$, and $\sigma_{Pt}^{cap} = 13\,\text{Å}$, were σ_{Co} increases with d_{Co} and deposition angle α as evidenced by the roughness increase (Figure 3, inset). The large value of σ_{Pt}^{cap} is due to the roughness of the underlying Co layer. The inset to Figure 3) shows representative data for three-layer stacks with increasing deposition angle, exhibiting a decrease in contrast (i.e., an increase in roughness).

The pole figure of the Co(0002) reflection on MgO(001) (**Figure 4**a) shows that there is intensity predominantly in the out-of-plane direction, i.e., a weak peak is visible at the origin in accordance with the out-of-plane XRD results in Figure 3. In contrast, for films on MgO(110) (Figure 4b), two pairs of relatively localized off-center spots with two-fold symmetry are found, inheriting the two-fold symmetry from the underlying MgO(110) substrate. Two equal intensity spots are located at $\phi = 0°/180°$ with $\chi \approx 45°$, and two stretched spots with different intensity at $\phi = 90°/270°$ with χ between 25° and 40°.

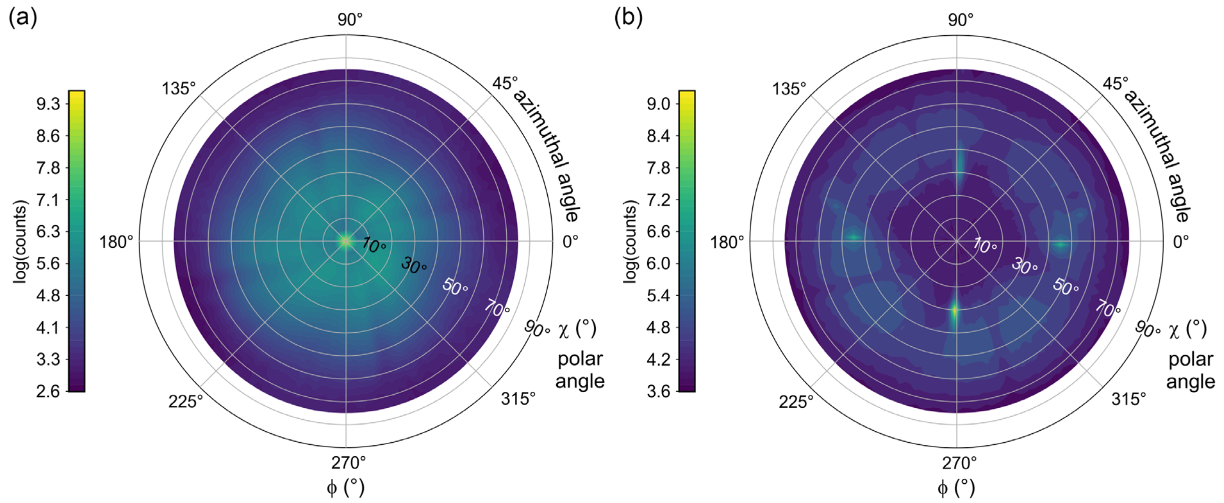

Figure 4. Pole figures with respect to the Co(0002) reflection at $2\theta = 44.4°$. a) 300 Å-thick Co film with $\alpha = 80°$, $\beta = 30°$ on MgO(001). b) 300-Å-thick Co film with $\alpha = 80°$, $\beta = 0°$ on MgO(110).

The corresponding MgO directions are not related to the observed Co[0002] reflections via any known epitaxial relationship, which means that the orientation of the columnar structures is, at least to some degree, the result of the GLAD process. For non-GLAD Co growth on epitaxial Pt(220) films on MgO(110) substrates, it is known that Co[0001] is parallel to Pt[001] and MgO[001] and Co[$11\bar{2}0$]||Pt[$1\bar{1}0$]||MgO[$1\bar{1}0$], i.e., Co($\bar{1}100$)||MgO(110).[25] In our case, the expected Co($\bar{1}100$) reflection was not observed. It is thus clear that while the MgO(110) substrate templates directional order onto the Co films, the deposition geometry is also affecting the film growth, however, without allowing for a direct control of the crystallographic orientation.

Three samples, two films on MgO(110) (**Figure 5**a,b) and one on MgO(001) (Figure 5c), were investigated in detail using TEM. Imaging was done from two in-plane directions, along the $\langle 00\bar{1}\rangle$ and the $\langle \bar{1}10\rangle$ zone axes of the MgO(110) substrates and along $\langle 100\rangle$ and $\langle 010\rangle$ of the MgO(001) substrate, respectively, corresponding to $\varphi = 0°$ and 90° for both types of substrates. The TEM images of the film on MgO(001) shown in Figure 5c are from a sample in which imprinting of the magnetic easy axis was successful. In contrast, Figure 5b,d are from a film on MgO(110) where the easy axis did not follow the imprinting direction. Interestingly, for certain deposition geometries, also films on MgO(110) can show successful imprinting, accompanied by a similar polycrystalline appearance (Figure 5a) as in the case of films on MgO(001). In all samples, analyzing the TEM images shown in Figure 5, we indeed found tilted columnar structures with a tilt angle that closely follows the tangent rule $\tan\alpha = 2\tan\gamma$, where γ is the tilt angle of the columns.[19,31] The geometry of the inclined columns, along with all relevant angles and dimensions, is shown as side and top views in Figure 2. Figure 5a,c exhibit $\gamma \approx 36°$ and 38°, which compares well with the expected 41° from the tangent rule for $\alpha = 60°$. For the film shown in Figure 5b,d, in contrast, the tilt is $\gamma \approx 45°$, which is further away from $\gamma = 70°$ expected for $\alpha = 80°$. Note that at these high angles, deviations from the rule can be expected. Along $\varphi = 0°$ (the $\langle 001\rangle$ zone axes), the columns are more difficult to see since they are viewed from a less steep angle and therefore appear wider. The projected column widths $w_{0°}$ and $w_{90°}$, visible along the two orthogonal cuts of the samples, were used to estimate the in-plane angle β (see Figure 2). Assuming a constant column width along the deposition direction, and crossing the ridges perpendicular to it, they are related through $w_{90°}/w_{0°} = \tan\beta$, where w_φ are the projected widths of the columns along the respective φ (or cut) directions (see Figure 2). For the three investigated samples, we found β to be 35(7)° (Figure 5a), 43(11)° (Figure 5b), and 29(9)° (Figure 5c), respectively, which are very close to the respective nominal imprinting angle β. The averages (standard deviations) for β are given, as determined by the analysis of the widths in the respective TEM image.

The most noticeable feature when comparing the TEM images of Co films on different MgO substrate systems is that the films on MgO(110) (**Figure 6**a) show a higher degree of crystallinity. Co films on MgO(001) (Figure 6b), in contrast, are characterized by polycrystallinity and a high degree of disorder. In Figure 6a,b, we show the corresponding diffractograms. For Co on MgO(110), clear features of hcp Co with its hexagonal motif can be seen, whereas, for Co on MgO(001), the diffractogram is disordered. It shows no clear symmetry from which the dominance of either

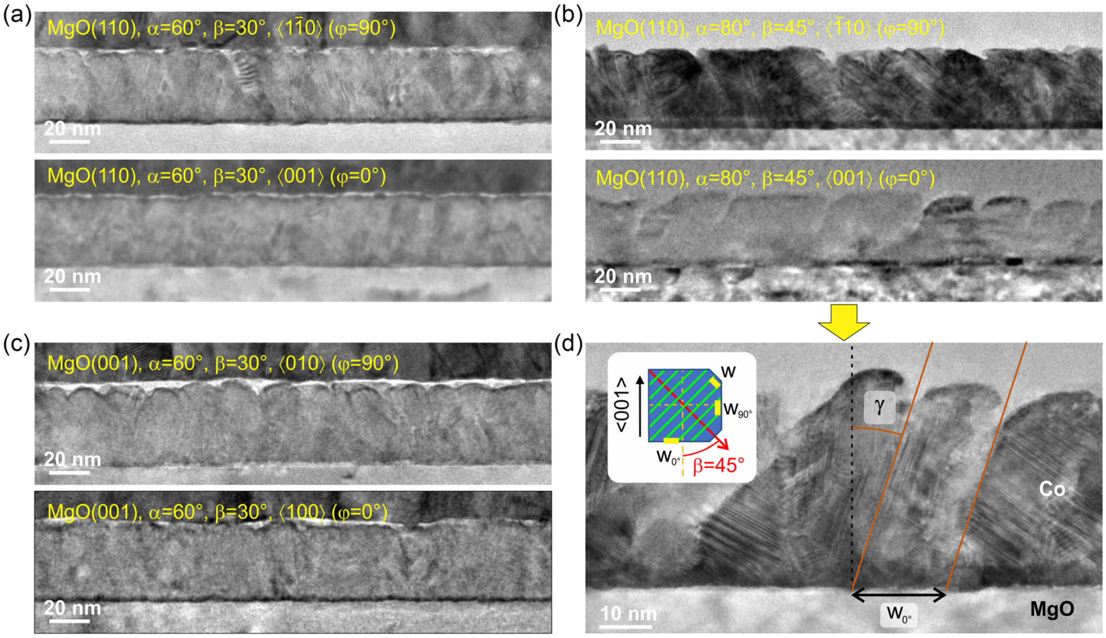

Figure 5. TEM images on Co films with a nominal thickness of 300 Å on a,b) MgO(110) and c) MgO(001) substrates. Above and below, the views along two different zone axes are shown. d) Close-up of the film on MgO(110) shown in b) along the $\langle 001\rangle$ zone axis. The tilt angle of the columns, γ, is indicated in the panel, along with the projected column width, $w_{0°}$, for the case of the $\langle 001\rangle$ zone axis. This geometry is further illustrated in the inset, which shows a top view of the MgO(110) substrate (see also Figure 2).

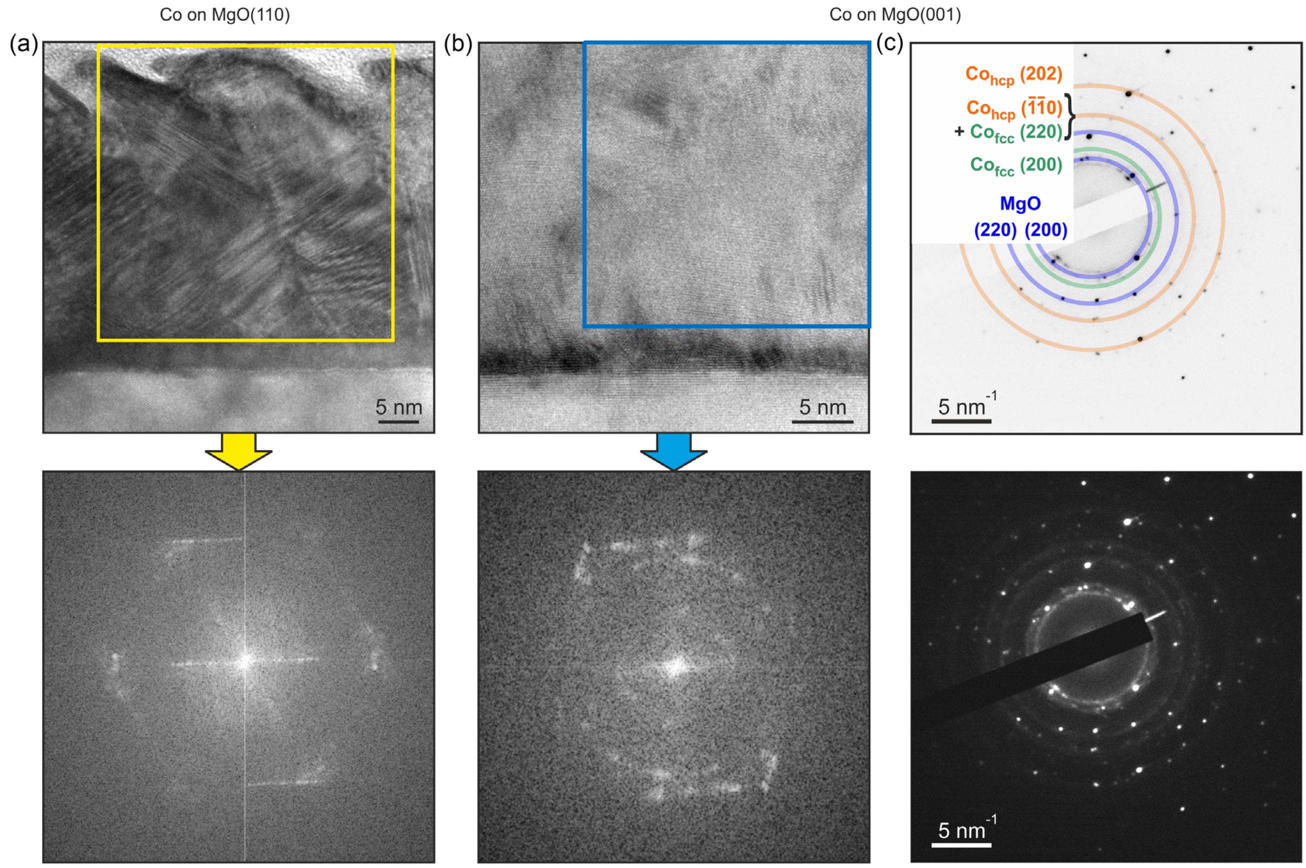

Figure 6. Phase analysis based on TEM images of Co films on a) MgO(110) and b,c) MgO(001) substrate systems. a) On MgO(110), the Co film (350 Å-thick, $\alpha = 45°$, $\beta = 45°$) is highly textured. The hcp phase of Co dominates, as can be seen by the hexagonal arrangements of the spots in the diffractogram. b) In contrast, on MgO(001), the Co film (344 Å-thick, $\alpha = 60°$, $\beta = 30°$) is nanocrystalline. The diffractogram from the blue area shown appears diffuse and shows no clear symmetry, consistent with the presence of a mixture of hcp and fcc Co. c) Selected area electron diffraction (SAED) pattern of the sample on MgO(001). The families of spots are labeled, and their positions are indicated by circles in the upper panel. Below, the same SAED image is shown with inverted contrast.

the hcp or fcc phase could be concluded. The multitude of spots instead points toward a mixed fcc-hcp phase. Indeed, when looking at the selected area electron diffraction images in Figure 6c taken of the sample, both Co phases are present. Note that for the structurally more ordered sample, magnetic imprinting failed, and the magnetic anisotropy rather followed the direction dictated by the MgO(110) substrate.

3.2. Magnetic Properties

Magnetization curves were recorded at different in-plane angles φ_H. As an example, the hysteresis loops for a 100 Å-thick Co film on MgO(001) with $\alpha = 60°$ and $\beta = 30°$ are shown in **Figure 7**a for various φ_H. We found the magnetization within the growth series (see Section 2.2) to always have its easy axis in-plane, which may be unexpected given the only weakly out-of-plane oriented hcp structure of the Co layer (as determined by XRD), however, not surprising considering the demagnetization factor of a thin film. For thin ($\leq$30 Å) Co films grown at room temperature on MgO(001), a four-fold magnetic anisotropy can be expected, with the easy axis directions being along Co $\langle 110 \rangle$.[32] The remanent magnetization, $\mathbf{M}_r$, was extracted from the loops at each in-plane angle φ_H and plotted as a function of φ_H in Figure 7b. The normalized remanence $\mathbf{M}_r/\mathbf{M}_s(\varphi_H)$ was fitted with a model for two-fold anisotropy, $\mathbf{M}_r/\mathbf{M}_s = A|\sin(\varphi_H + \varphi_{HA})| + B$, where A, B, and φ_{HA} are fitting parameters. The fit to the data points shown in Figure 7b reveals the easy axis of magnetization at $\varphi_{EA} = 121°$, which is at 90° from the hard axis, i.e., $\varphi_{EA} = \varphi_{HA} + 90°$.

Figure 8 shows anisotropy plots from three 50-Å-thick Co films deposited under the same conditions on MgO(001), only varying in β. For each film, the magnetic easy axis is always at 90° from the imprinted axis at β, thereby demonstrating perfect control of the magnetic anisotropy using GLAD. In total, we deposited 14 samples on MgO(001) with varying d_{Co} and α, all showing full anisotropy control via β (with the easy axis at $90° + \beta$).

In contrast, for films on MgO(110), the situation is more complicated. For example, when depositing 50 Å-thick Co films ($\alpha = 60°$, $\beta = 30°$) on MgO(110) under nominally identical conditions, we obtained in only a few cases almost perfect anisotropy control with $\varphi_{EA} = 138°$, while most of the samples showed φ_{EA} close to 180°. The latter has the easy axis essential almost

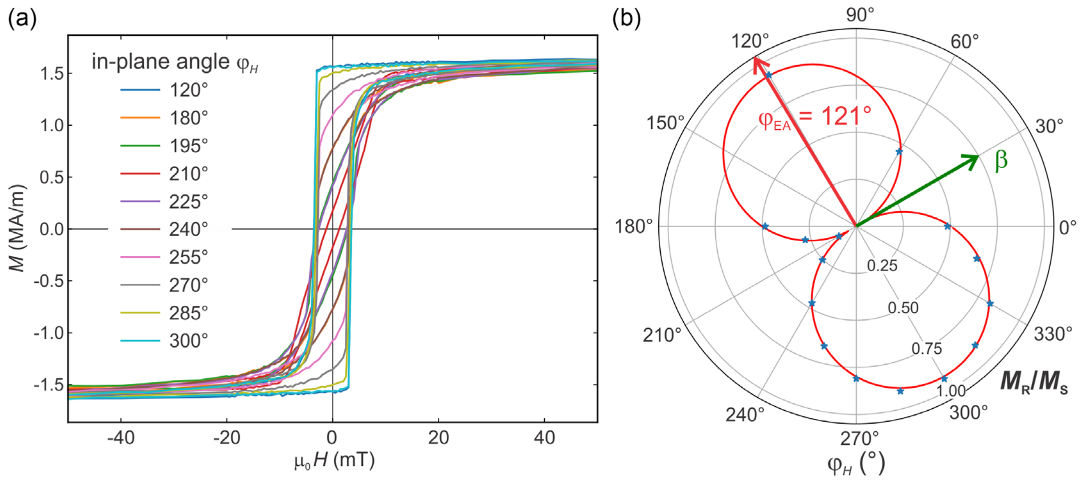

Figure 7. a) Hysteresis loops recorded with VSM for fields applied under different in-plane angles, φ_H, for a 100 Å-thick Co film on MgO(001) ($\alpha = 60°$, $\beta = 30°$). b) Corresponding anisotropy plot. The dots represent the normalized remanent magnetization $\mathbf{M}_R/\mathbf{M}_S$ versus in-plane angle φ_H relative to the [001]-direction of the MgO substrate. The red curve is a fit to the data using a two-fold anisotropy model, with the red arrow pointing along the easy axis. The imprinted easy axis is expected to be at 90° from the in-plane deposition axis (green arrow). In this case, $\beta = 30°$ and the resulting $\varphi_{EA} = 121°$ agrees well with the expected value.

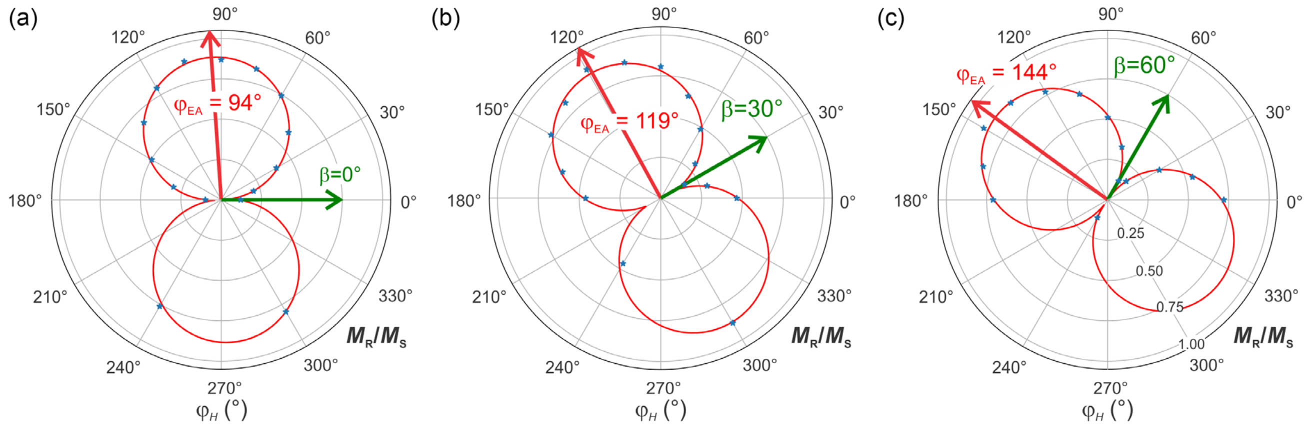

Figure 8. Anisotropy plots for Co films on MgO(001) with $\alpha = 60°$ and $d_{Co} = 50$ Å, but deposited at different in-plane angles β, i.e., at a) 0°, b) 30°, and c) 60°. The good agreement between the respective ($\beta + 90°$) and φ_{EA} demonstrate successful imprinting.

perfectly aligned with the ⟨001⟩ direction of the substrate (180°), i.e., the substrate orientation governs the magnetic anisotropy of the film irrespective of the GLAD angle. The situation was the same for other combinations of d_{Co}, α, and β, and only occasionally anisotropy control was achieved, i.e., the is no correlation between anisotropy control and the deposition parameters.

In principle, for thin films, one can expect a thickness dependence of the in-plane uniaxial anisotropy energy K_U, usually increasing with decreasing film thickness d.[16,22] A measure of the anisotropy energy is given by the difference in remanent magnetization $\Delta(\mathbf{M}_R/\mathbf{M}_S)$ between the easy and hard axes. Plots of $\Delta(\mathbf{M}_R/\mathbf{M}_S)$, which are proportional to the anisotropy energy, are shown as a function of d_{Co} and the deposition angle α in **Figure 9**a,b, respectively. For films on MgO(001), the observed thickness trend agrees with the expectation that thinner films have higher anisotropy energy than thicker ones due to their shape anisotropy. In the XRD spectra of the thicker films (>300 Å), signs of increased crystallinity of the Co layer were found (see Figure 3), which could be the cause for the decrease of $\mathbf{M}_R/\mathbf{M}_S$ as well. Note that the error is larger for thinner samples since there is less material to measure, and the relative error in fitted thickness used to calculate the magnetic moments is larger. In terms of deposition angle, a complex dependence of K_U on α has been reported, with the energy maximum found for an intermediate angle. For $d_{Co} = 50$ Å, the smallest energy is found for $\alpha = 50°$, and it is continuously increasing for 60° and 70°until there is a decrease at very high angles (80°).

In contrast, films grown on MgO(110) show no clear trend. The anisotropy energy of most films on MgO(110) is several times larger than those on MgO(001), demonstrating that the anisotropy, in this case, is caused by a much stronger effect, competing with the imprinted anisotropy from GLAD. This effect clearly originates from the substrates, as the easy axis always points along the ⟨001⟩ direction of MgO(110). Note that in rare cases, we found the anisotropy of films on MgO(110) to be comparable to those on Mg(001); however, we did not

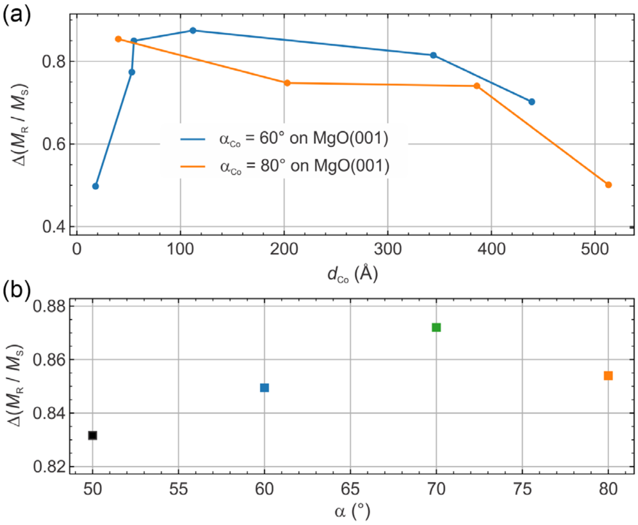

Figure 9. Plots of the difference of remanent magnetization along the easy and hard axes $\Delta(\mathbf{M}_R/\mathbf{M}_S)$, which is proportional to the anisotropy energy, as a function of a) film thickness and b) deposition angle for a 50 Å-thick Co film on MgO(001).

study their behavior in more detail due to the inconsistent dependencies.

3.3. Discussion

By employing the GLAD process,[19–21] shadowing will lead to tilted columnar growth. The resulting structural anisotropy of the tilted columns, and possibly also of their noncircular cross-section,[22] will further affect their magnetic anisotropy. However, the overall magnetic properties of the films not only stem from the columnar magnetic properties but are also determined by the shape and surface anisotropies of the film (i.e., depending on the film thickness) and substrate interactions. For example, for Fe films on amorphous substrates, high-incidence angles result in needle-like columns and low-incidence angles in an extended wall-like structure (perpendicular to the plane of incidence), with the in-plane magnetic easy axis parallel and perpendicular to the incidence plane, respectively.[16] Note that the columnar structures in thicker films have a defined crystallographic orientation, which is dependent on the growth rate.[16] For ultrathin Fe layers on sapphire, in contrast, where the films are polycrystalline, full control of the in-plane magnetic anisotropy has been achieved via the deposition angle.[18]

The behavior of Co films can be expected to be different from that of Fe films, resulting from differences in magnetocrystalline anisotropy. However, note that while polycrystalline Co has a larger magnetocrystalline anisotropy than Fe,[18] the change of crystal structure in Co columns from hcp to fcc can lead to a lower anisotropy.[22] For example, for high-incidence angle deposited Co films on amorphous substrates, a transition in the magnetic anisotropy was observed at a critical thickness of 300 Å, below which the easy axis is in-plane and above which the easy axis is tilted away from the film plane.[22] The tilted easy axis of the thicker films, which is confined to the incidence plane, has been tied to the microstructure of the fcc Co columns. In contrast, the in-plane anisotropy of the thinner films was explained by the fact that instead of pronounced columns, they are dominated by elongated nuclei. Given the low magnetic anisotropy of randomly oriented fcc Co grains, the shape anisotropy of the elliptic nuclei is believed to be the reason for their in-plane easy axis perpendicular to the incidence plane.[22] The presence of elongated nuclei in the early stages of film growth was determined by atomic force microscopy (AFM) imaging.

In our Co films on MgO(001), in which imprinting was achieved with the easy axis always perpendicular to the in-plane deposition angle, we find no evidence of uniaxially elongated Co nuclei from AFM imaging, which could explain this observation via the shape anisotropy tied to the microstructure. Further, while the in-plane anisotropy increases with Co film thickness (Figure 9), no transition of the magnetic anisotropy from in-plane toward the out-of-plane direction is observed, which would have been the result of pronounced columnar growth pulling the easy axis out of the plane. As can be seen for ≈ 300 Å-thick Co films on MgO(001) in Figure 5c and 6b,c, the columns are not very pronounced compared to the TEM image shown in ref. [22].

Our Co films on MgO(001) show a two-fold in-plane anisotropy (Figure 8), strictly tied to be perpendicular to the in-plane deposition angle. This means that the MgO(001) substrate with its four-fold symmetry has no direct effect on the structural properties of the Co films, as it would be the case for physical vapor-deposited films under normal incidence.[32] In contrast, Co films on MgO(110) show a strong influence of the substrate on the magnetic properties, which makes this substrate orientation unsuitable for GLAD deposition. It should be noted that successful imprinting has been achieved for extreme angles ($\alpha = 80°$); however, given the observed differences in magnetic properties of nominally almost identically grown films, it appears that other effects, e.g., the polishing and surface quality of the commercial substrates, have a stronger influence on the film parameters than any of the GLAD parameters.

4. Conclusions

Here, we have demonstrated the control of the in-plane magnetic anisotropy of Co thin films on MgO(001) using GLAD. By carrying out VSM measurements with varying azimuthal angles, we found that the direction of the magnetic easy axis is always perpendicular to the in-plane deposition angle β. The strength of the anisotropy energy, as estimated by the difference in remanent magnetization between the easy and hard axes, is determined by the film thickness and the GLAD angle. In contrast, on MgO(110), the crystalline anisotropy dominates over the imprinting effects, yielding a magnetic anisotropy that is dictated by the substrate. Therefore, the easy axis is along the substrate's ⟨001⟩ direction, independent of the film thickness, the GLAD, or the deposition angle. While GLAD results in a tilted columnar microstructure on both MgO(001) and (110) substrates, the anisotropy induced by the substrate, if present, is stronger than the GLAD-induced anisotropy tied to the microstructure. The control of the magnetic anisotropy of magnetic layers on crystalline substrates is of great importance for magnetic device fabrication, and industry-compatible GLAD-based magnetron sputtering is a promising approach.

Acknowledgements

The authors acknowledge the Engineering and Physical Sciences Research Council (EPSRC) under (grant nos. EP/P021190/1, EP/P020151/1, EP/P02047X/1, and EP/N032128/1). The work of D.G.N. was supported by the EPSRC Centre for Doctoral Training in Metamaterials under (grant no. EP/L015331/1). We would like to thank G. Stenning and D. Nye for their help with the Rigaku SmartLab in the Materials Characterisation Laboratory at the ISIS Neutron and Muon Source. We thank Diamond Light Source for access and support in the use of the electron Physical Science Imaging Centre (ePSIC) on instrument E03 (proposal numbers MG23285-39 through 49) that contributed to the results presented here, and RCaH for access to the TEM and deposition tools in preparation for FIB milling.

Conflict of Interest

The authors declare no conflict of interest.

Data Availability Statement

The data that support the findings of this study are available from the corresponding author upon reasonable request.

Keywords

Co thin films, glancing angle deposition, magnetic anisotropy, magnetron sputtering, MgO substrate

Received: January 4, 2023
Revised: February 27, 2023
Published online: April 7, 2023

---

[1] M. T. Johnson, P. J. H. Bloemen, F. J. A. den Broeder, J. J. D. Vries, *Rep. Prog. Phys.* **1996**, *59*, 1409.
[2] C. Chappert, A. Fert, F. N. Van Dau, *Nat. Mater.* **2007**, *6*, 813.
[3] M. N. Baibich, J. M. Broto, A. Fert, F. N. Van Dau, F. Petroff, P. Eitenne, G. Creuzet, A. Friederich, J. Chazelas, *Phys. Rev. Lett.* **1988**, *61*, 2472.
[4] G. Binasch, P. Grünberg, F. Saurenbach, W. Zinn, *Phys. Rev. B* **1989**, *39*, 4828.
[5] C. Rizal, B. Moa, B. Niraula, *Magnetochem.* **2016**, *2*, 22.
[6] B. Cui, D. Yu, Z. Shao, Y. Liu, H. Wu, P. Nan, Z. Zhu, C. Wu, T. Guo, P. Chen, H.-A. Zhou, L. Xi, W. Jiang, H. Wang, S. Liang, H. Du, K. L. Wang, W. Wang, K. Wu, X. Han, G. Zhang, H. Yang, G. Yu, *Adv. Mater.* **2021**, *33*, 2006924.
[7] G. van der Laan, *J. Phys. Condens. Matter* **1998**, *10*, 3239.
[8] J. Fassbender, G. Güntherodt, C. Mathieu, B. Hillebrands, R. Jungblut, J. Kohlhepp, M. T. Johnson, D. J. Roberts, G. A. Gehring, *Phys. Rev. B* **1998**, *57*, 5870.
[9] N. A. Morley, M. R. J. Gibbs, E. Ahmad, I. Will, Y. B. Xu, *J. Magn. Magn. Mater.* **2006**, *300*, 436.
[10] J. Thomassen, F. May, B. Feldmann, M. Wuttig, H. Ibach, *Phys. Rev. Lett.* **1992**, *69*, 3831.
[11] C. A. F. Vaz, S. J. Steinmuller, J. A. C. Bland, *Phys. Rev. B* **2007**, *75*, 132402.
[12] M. O. Liedke, B. Liedke, A. Keller, B. Hillebrands, A. Mücklich, S. Facsko, J. Fassbender, *Phys. Rev. B* **2007**, *75*, 220407.
[13] K. Chen, R. Frömter, S. Rössler, N. Mikuszeit, H. P. Oepen, *Phys. Rev. B* **2012**, *86*, 064432.
[14] M. Dąbrowski, M. Cinal, A. K. Schmid, J. Kirschner, M. Przybylski, *Phys. Rev. B* **2019**, *99*, 184420.
[15] J. Fassbender, J. McCord, *J. Magn. Magn. Mater.* **2008**, *320*, 579.
[16] K. Ozawa, T. Yanada, H. Masuya, M. Sato, S. Ishio, M. Takahashi, *J. Magn. Magn. Mater.* **1983**, *35*, 289.
[17] S. van Dijken, G. Di Santo, B. Poelsema, *Appl. Phys. Lett.* **2000**, *77*, 2030.
[18] K. Schlage, L. Bocklage, D. Erb, J. Comfort, H.-C. Wille, R. Röhlsberger, *Adv. Funct. Mater.* **2016**, *26*, 7423.
[19] M. M. Hawkeye, M. J. Brett, *J. Vac. Sci. Technol. A* **2007**, *25*, 1317.
[20] *Handbook of Deposition Technologies for Films and Coatings*, 3rd ed. (Eds: M. T. Taschuk, M. M. Hawkeye, M. J. Brett, P. M. Martin), William Andrew Publishing, Boston **2010**, pp. 621–678.
[21] A. Barranco, A. Borras, A. R. Gonzalez-Elipe, A. Palmero, *Prog. Mater. Sci.* **2016**, *76*, 59.
[22] A. Lisfi, J. C. Lodder, H. Wormeester, B. Poelsema, *Phys. Rev. B* **2002**, *66*, 174420.
[23] C.-F. Pai, L. Liu, Y. Li, H. W. Tseng, D. C. Ralph, R. A. Buhrman, *Appl. Phys. Lett.* **2012**, *101*, 122404.
[24] I. M. Miron, K. Garello, G. Gaudin, P.-J. Zermatten, M. V. Costache, S. Auffret, S. Bandiera, B. Rodmacq, A. Schuhl, P. Gambardella, *Nature* **2011**, *476*, 189.
[25] R. Thompson, J. Ryu, Y. Du, S. Karube, M. Kohda, J. Nitta, *Phys. Rev. B* **2020**, *101*, 214415.
[26] A. Manchon, J. Železný, I. M. Miron, T. Jungwirth, J. Sinova, A. Thiaville, K. Garello, P. Gambardella, *Rev. Mod. Phys.* **2019**, *91*, 035004.
[27] T. Jin, G. J. Lim, H. Y. Poh, S. Wu, F. Tan, W. S. Lew, *ACS Appl. Mater. Interfaces* **2022**, *14*, 9781.
[28] T. Nozaki, M. Konoto, T. Nozaki, H. Kubota, A. Fukushima, S. Yuasa, *AIP Adv.* **2020**, *10*, 035130.
[29] A. Frisk, *Ph.D. thesis*, Uppsala University, Uppsala, Sweden **2016**, http://urn.kb.se/resolve?urn=urn:nbn:se:uu:diva-305523 (accessed: March 2023).
[30] M. Björck, G. Andersson, *J. Appl. Crystallogr.* **2007**, *40*, 1174.
[31] J. M. Nieuwenhuizen, H. B. Haanstra, *Philips Tech. Rev.* **1966**, *27*, 87.
[32] M. J. M. Pires, A. A. C. Cotta, M. D. Martins, A. M. A. Silva, W. A. A. Macedo, *J. Magn. Magn. Mater.* **2011**, *323*, 789.